Applied Catalysis B: Environmental 204 (2017) 324–334

Contents lists available at ScienceDirect

Applied Catalysis B: Environmental

journal homepage: www.elsevier.com/locate/apcatb

Research paper

# Enhanced mechanism of the photo-thermochemical cycle based on effective Fe-doping $TiO_2$ films and DFT calculations

Chenyu Xu, Yanwei Zhang*, Jingche Chen, Jiayi Lin, Xuhan Zhang, Zhihua Wang, Junhu Zhou

*State Key Laboratory of Clean Energy Utilization, Zhejiang University, Hangzhou 310027, China*

ARTICLE INFO

*Article history:*
Received 23 August 2016
Received in revised form
10 November 2016
Accepted 15 November 2016
Available online 16 November 2016

*Keywords:*
Photo-thermochemical cycle
Oxygen vacancies
Water splitting
First-principles calculations
Fe-doped oxide

ABSTRACT

To study the mechanism of the photo-thermochemical cycle (PTC), titanium dioxide ($TiO_2$) and Fe-doped $TiO_2$ films were produced using a sol-gel method and applied in the PTC for water splitting. A comparison of $H_2$ production shows that Fe-doped $TiO_2$ performed better than undoped $TiO_2$. Scanning electron microscopy (SEM), transmission electron microscopy (TEM), energy-dispersive X-ray spectroscopy (EDXS), X-ray diffraction (XRD) and Brunauer–Emmett–Teller (BET) were used to assess the crystal structure and morphology of the films. UV–vis diffuse reflectance spectra (UV–vis DRS), photoluminescence (PL) and X-ray photoelectron spectroscopy (XPS) analyses were also conducted to investigate the charge transfer and reaction mechanisms on the $TiO_2$ surface. Density functional theory (DFT) calculations related to the anatase (101) surface of $TiO_2$ and Fe-doped $TiO_2$ were performed to verify and provide guidance for enhancing the PTC mechanism. As a result, several key factors of the mechanism have been clarified and a reaction mechanism has been proposed for the whole cycle.

© 2016 Elsevier B.V. All rights reserved.

## 1. Introduction

The increasing interest in environmentally friendly energy provides motivation for researchers of novel energy materials and conversion systems. Hydrogen, a clean energy carrier, holds great potential as a future alternative fuel [1–3]. Harnessing solar energy for the production of clean hydrogen by water splitting represents an attractive yet challenging approach for sustainable energy generation [4–6]. Two-step thermochemical cycles based on metal oxides (primarily Zn/ZnO, $Ce_2O_3/CeO_2$, $FeO/Fe_3O_4$, and $SnO/SnO_2$) and starting from two massive natural resources such as solar energy and water are a notable approach for the environmentally friendly production of hydrogen [7–10]. The following chemical reaction can be used to describe the two-step thermochemical cycle for $H_2O$ dissociation:

$$M_xO_y \rightarrow M_xO_{y-1} + 1/2O_2(g)(\text{thermochemistry}, > 1273\,K) \quad (1)$$

$$M_xO_{y-1} + H_2O(g) \rightarrow M_xO_y + H_2(g)(\text{thermochemistry}, > 573\,K) \quad (2)$$

Its simple procedure, recyclability, effectiveness and utilization of energy make this a promising and attractive system. Hence, many researchers have attempted to optimize this technique. However, the high cycle temperature (>1273 K) is difficult to decrease without sacrificing the other advantages of this method [11].

A novel photo-thermochemical cycle (PTC) for the dissociation of $H_2O$ or carbon dioxide ($CO_2$) has been reported by Zhang et al. [12,13] They introduced the photochemical method into the two-step thermochemical cycle, achieving an impressive decrease of the cycle temperature. The PTC for $H_2O$ splitting consists of two reactions:

$$M_xO_y \rightarrow M_xO_{y-1} + 1/2O_2(g)(\text{photochemistry}, > 300\,K) \quad (3)$$

$$M_xO_{y-1} + H_2O(g) \rightarrow M_xO_y + H_2(g)(\text{thermochemistry}, > 573\,K) \quad (4)$$

Photo-induced oxygen vacancies ($V_O$) are produced on the surface of the metal oxide under UV in the first step (Reaction (3)). The photo-induced $V_O$ are then used to dissociate $H_2O$ below 873 K in the second thermochemical step (Reaction (4)), which is similar to the second step in the thermochemical cycle. As a result, the overall reaction is the dissociation of $H_2O$ and the production of $H_2$ and $O_2$. Therefore, the PTC has characteristics of both thermochemistry and photochemistry, thereby utilizing both solar heat and light, as shown in Fig. S1.

Since the first report in 1972 that $TiO_2$ can dissociate water into $H_2$ and $O_2$ through photocatalysis, $TiO_2$ has been widely studied as a semiconductor catalyst because of its excellent stability, low cost, high resistance to corrosion and nontoxicity [14–17]. Zhang et al.

* Corresponding author.
*E-mail address:* zhangyw@zju.edu.cn (Y. Zhang).

http://dx.doi.org/10.1016/j.apcatb.2016.11.027
0926-3373/© 2016 Elsevier B.V. All rights reserved.

used $TiO_2$ to dissociate water and $CO_2$ in a PTC, thereby confirming the possibility of the PTC. They proposed a possible reaction mechanism after an in-depth investigation [12,13]. Their proposed PTC mechanism suggests that photogenerated electrons and holes react with metal ions and oxygen ions, respectively, in the first photostep. Then, $V_O$ is formed to reduce $H_2O$ or $CO_2$ on the surface of the metal oxide in the second thermal step. Finally, $H_2$ or CO is produced when the whole cycle is completed.

Future directions for the development of PTC materials include the achievement of a wider photoresponse range, a lower electron-hole recombination rate and lower formation energy of $V_O$. The physical properties of $TiO_2$ include a wide band gap that can harvest only a portion of the visible-light spectrum. Furthermore, the high rate of recombination of electron-hole pairs causes low photoreaction efficiency in $TiO_2$ [18].

Doping of $TiO_2$ with metals such as transition-metal ions (Fe, Zn, V, Cr, ...) and noble-metal nanoparticles (Pt, Au, Ag, ...) is being widely investigated to overcome the shortcomings of $TiO_2$ [19,20]. And many literatures reported that anti-sintering stability of metal oxide may be improved by transition-metal ions (Fe, Ce, Cr, Zr, ...) doping. Among these, the iron(III) ions have been considered an appropriate candidate to dope $TiO_2$ for its sintering resistance and good photocatalytic performance [21,22]. Because of the similar ionic radii of $Fe^{3+}$ (0.69 Å) and $Ti^{4+}$ (0.745 Å) which $Fe^{3+}$ can be easily incorporated into the $TiO_2$ crystal lattice [23]. Moreover, numerous studies have shown that a new energy level, shallow charge-trapping centres and $V_O$ can be formed by $Fe^{3+}$ ions on the surface of $TiO_2$, resulting in a wider photoresponse range, a more intense charge transfer reaction and a lower bond energy on the surface, respectively [24]. Notably, however, a large amount of $Fe^{3+}$ leads to a higher electron-hole recombination rate, thereby reducing the photocatalytic activity. Because of the varied and inconsistent results, the photoactivity enhancement of $Fe^{3+}$-doped $TiO_2$ has been controversial [25].

In this research, we used $TiO_2$ and Fe-doped $TiO_2$ prepared by a sol-gel method to augment the proposed mechanism of PTC by comparing various physical and chemical properties. Although the possible reaction mechanism of PTC has been investigated, many issues remain unresolved, such as the relationship among the enhancement of the electron-hole separation rate, a lower $V_O$ formation energy and the reaction performance. We prepared Fe-doped $TiO_2$ via a sol-gel method as a representative $TiO_2$ material doped with metal ions. We selected 0.5 wt% Fe-doped $TiO_2$ for the same reason reported in a large number of previous studies: the optimal mass fraction ratio of Fe to Ti is in the range from 0.1% to 1% in traditional photocatalysis [23,24,26]. Furthermore, we conducted measurements over several cycles to confirm the augmented $H_2$ production and to investigate the action of Fe-doped $TiO_2$ in the PTC under various conditions. Finally, we performed first-principles calculations on the anatase (101) surface of $TiO_2$ and Fe-doped $TiO_2$ to verify and enhance the proposed mechanism [27,28].

## 2. Experimental

### 2.1. Chemicals and materials

Tetrabutyl titanate ($Ti(OC_4H_9)$, Sinopharm Chemical Reagent Co., Ltd.), glacial acetic acid ($CH_3COOH$, Sinopharm Chemical Reagent Co., Ltd.), anhydrous ethanol (EtOH, Sinopharm Chemical Reagent Co., Ltd.) and iron nitrate ($Fe(NO_3)_3{\cdot}9H_2O$, Sinopharm Chemical Reagent Co., Ltd.) were all of analytical grade. All reagents were used as received, without further purification. Deionized water was used in all experiments.

### 2.2. sol-gel preparation of $TiO_2$ and Fe-doped $TiO_2$ thin films

A typical sol-gel synthesis procedure was used to prepare $TiO_2$ and Fe-doped $TiO_2$ in this work. Ten millilitres of tetrabutyl titanate was dissolved into 30 ml absolute ethanol; the resulting solution is hereafter referred to as solution A. Solution B was prepared by mixing 4 ml glacial acetic and 5 ml deionized water with 30 ml absolute ethanol. Iron (III) nitrate (59.6 mg) was dissolved into solution B to obtain solution C. To prepare $TiO_2$ and the Fe-$TiO_2$ precursor, solutions B and C were added slowly to two separate preparations of solution A under continuous stirring. The two resulting mixtures were aged for 24 h at room temperature under vigorous stirring. After the obtained gels were dried at 383 K, the resulting xerogels were ground into powders using an agate mortar, calcined at 773 K (heating rate = 2 K/min) for 3 h and cooled under an air atmosphere. Fifty milligrams of the produced $TiO_2$ and Fe-doped $TiO_2$ powders were dissolved into tubes with 5 ml deionized water and ultrasonically dispersed for 10 min. Then, the two suspensions were poured into two preheated, round quartz saucers (diameter of 5 cm) at 383 K for 3 h. Finally, layers of the $TiO_2$ film and Fe-doped $TiO_2$ film were deposited and formed on the quartz saucers, respectively.

### 2.3. Photo-thermochemical cycling experiments

An elaborate experimental platform was designed in this study, as shown in Fig. 1. $TiO_2$ and Fe-doped $TiO_2$ films were preheated at 973 K for 4 h under a pure $O_2$ atmosphere to remove adsorbed organics (e.g., residual carbon) and volatile compounds (e.g., residual moisture) in the pretreatment stage. A cylindrical stainless steel reactor (volume of approximately 50 ml) was used, and the sample films were positioned on the floor. Quartz and stainless steel covers were fabricated for the cylindrical reactor for the photochemical and thermochemical processes, respectively.

In the first stage of the PTC, a quartz cover was used on the stainless steel reactor. Argon gas, which served as a protective atmosphere to prevent reoxidation of the sample films, was fed into the reactor at a flow rate of 100 ml/min. A mercury lamp (500 W) was used as the UV light source (>254 nm) to illuminate the thin-film samples for 0–1 h at room temperature. After the photochemical reaction, the quartz cover on the reactor was quickly replaced with a stainless steel cover because of the stress induced by the high-temperature steam. Then, Ar gas was passed through the other gas circuit into a water bubbler heated in a thermostatic water bath at 343 K. After the gaseous mixture was passed through the system for 30 min, the reactor was purged with the mixture and a wet Ar atmosphere was thus formed. The gas valves were then closed to form an airtight chamber. After the reactants were heated at a known temperature below 973 K for 1 h, the gaseous products were generated and detected using a gas chromatograph (Agilent 7820A) equipped with a thermal conductivity detector (TCD).

### 2.4. Analysis and characterization methods

The SEM images were obtained using an FEISIRION-100 thermal field-emission scanning electron microscope. The TEM and EDAX micrographs were recorded on an FEI Tecnai G2 F20 S-TWIN instrument using an acceleration voltage of 200 kV. The BET specific surface area were determined at liquid nitrogen temperature (77 K) using a Quantachrome Autosorb Automated Gas Sorption System. The XRD patterns were acquired with a Cu $K_\alpha$ radiation source ($K_\alpha$ = 1.540598 Å) operated at 40 kV and 100 mA. The diffraction patterns were recorded over the 2θ range $10^\circ \le 2\theta \le 90^\circ$ at intervals of 0.02° and with 0.3 s time steps. The crystal sizes of the samples were calculated using the Debye–Scherrer equation. Electron–hole recombination in the prepared catalysts was investigated on the basis of their photoluminescence (PL) emission

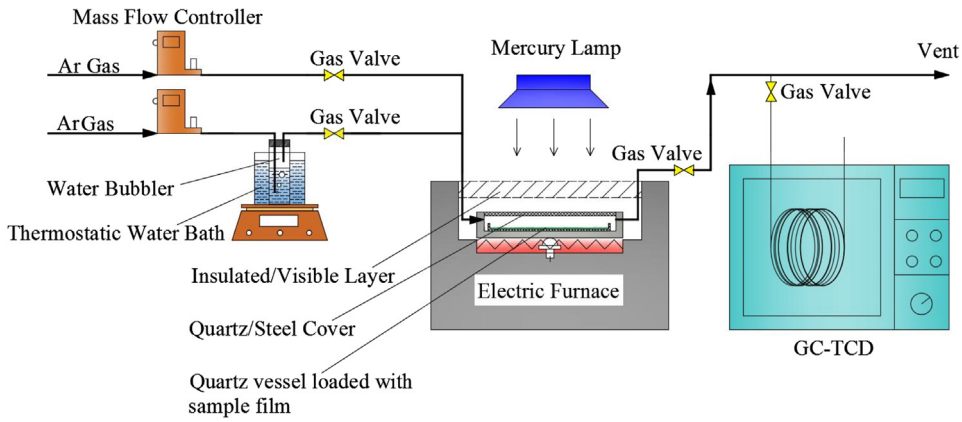


**Fig. 1.** Experimental platform for $H_2O$ splitting of PTC.

spectra, which were collected at room temperature on an Edinburgh Instruments FLS 920 equipped with a 325 nm excitation light. To analyse the band-gap energy values of the samples, UV–vis diffuse reflectance spectra (UV–vis DRS) of $TiO_2$ and Fe-doped $TiO_2$ nanocomposite films were obtained using a UV–vis spectrophotometer (UV–vis, 300–600 nm, SHIMADZU UV-3600, Japan). The XPS data were obtained with an ESCA Lab 250Xielectron spectrometer from Thermo Fisher Scientific. All binding energies were referenced to the C 1s peak (284.6 eV), which was used to determine the adventitious carbon in the test sample preparation.

### 2.5. Theoretical calculations

All the calculations were performed using density functional theory (DFT) on the basis of PAW-PBE potentials implemented in the VASP 4.6 program. An ultra soft pseudo potential was used to describe electron–ion interactions with kinetic energy cutoffs of 400.0 eV. In energy calculations, the K-point grid was set to $3 \times 3 \times 1$. The convergence threshold for self-consistent-field iteration was set to $10^{-4}$ eV. All the atomic positions were fully optimized until all components of the residual forces were less than 0.01 eV/Å. The description of exchange-correlation effects utilizes the local density approximation (LDA) and general gradient approximation (GGA), which always leads to a severe underestimation of band gaps for transition metals. To compensate for this limitation, GGA + U were used in this work. The Coulomb correlation interaction of Ti and Fe 3d electrons was taken into account. According to the XRD results, the majority of the exposed crystal faces in the samples were $TiO_2$ anatase (101), which was customarily selected as the representative crystal face in all calculations [29]. All the energy calculations adopted the values U = 5.00 eV for Fe 3d and U = 8.20 eV for Ti 3d. A slab of $Ti_{24}O_{48}$ with a surface area of $10.89 \times 7.55$ Å$^2$ was selected, and the slab thickness were 3 layers (see Fig. 2(a)). More discussions about adopting U values (Fig. S2 and Table S1) and slab thickness (Fig. S3) were shown in Supporting information. Four types of oxygen and two types of titanium were included: the bridging two-fold coordinated oxygen atom ($O_{2C}$), three types of three-fold coordinated oxygen atom ($O^1{}_{3C}$, $O^2{}_{3C}$, $O^3{}_{3C}$), and five/six-fold coordinated titanium atoms ($Ti_{5C}$/$Ti_{6C}$), as shown in Fig. 2.

## 3. Results and discussion

### 3.1. Performance of photo-thermochemical experiments

To assess the influence of photochemical time, thermochemical time, thermochemical temperature and stability of cycles, we

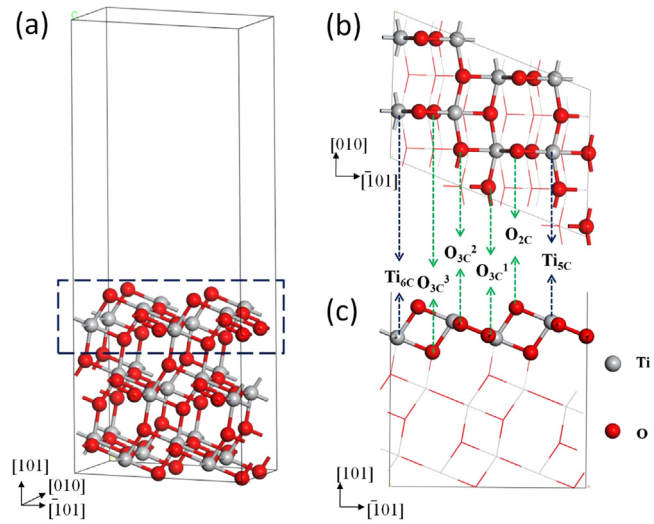


**Fig. 2.** Relaxed structure of the $Ti_{24}O_{48}$ surface cell with a surface area of $10.89 \times 7.55$ Å$^2$. The first layer is in the dashed-line rectangle.

conducted a series of experiments for comparing $TiO_2$ and Fe-doped $TiO_2$, as shown in Fig. 3. The $H_2$ yield in the PTC increased in the case of Fe-doped $TiO_2$ compared to the case of $TiO_2$. This increase may indicate that more available $V_O$ was produced on the surface of Fe-doped $TiO_2$. Six independent cycles were studied for a series of times (from 10 min to 60 min in 10 min increments) under an Ar atmosphere and under heating at 873 K for 1 h in a wet Ar atmosphere, as shown in Fig. 3(a). A substantial increase in $H_2$ production was observed from 10 min to 30 min, whereas $H_2$ production changed only slightly from 30 min to 60 min. This result indicates that the $V_O$ concentration increased with increasing irradiation time and that the total amount of created $V_O$ was maximized at 30 min and 40 min for Fe-doped $TiO_2$ and $TiO_2$, respectively. To investigate the influence of thermochemical time, six independent cycles were performed; the results are shown in Fig. 3(b). Fe-doped $TiO_2$ and $TiO_2$ were irradiated for 30 min and 40 min, respectively, and heated for 10 min, 20 min, 30 min, 40 min, 50 min and 60 min (in this order) at 873 K. The maximum output of $H_2$ was achieved at 60 min for Fe-doped $TiO_2$ and at 50 min for $TiO_2$. This result may be due to the increased amount of $V_O$ in Fe-doped $TiO_2$, which would require more time for consumption. Fig. 3(c) shows that the $H_2$ yield increased with increasing heating temperature during the thermochemical step in five independent PTC experiments. Fe-doped $TiO_2$ was illuminated for 30 min and heated for 60 min, whereas $TiO_2$ was illuminated for 40 min and heated for 50 min.

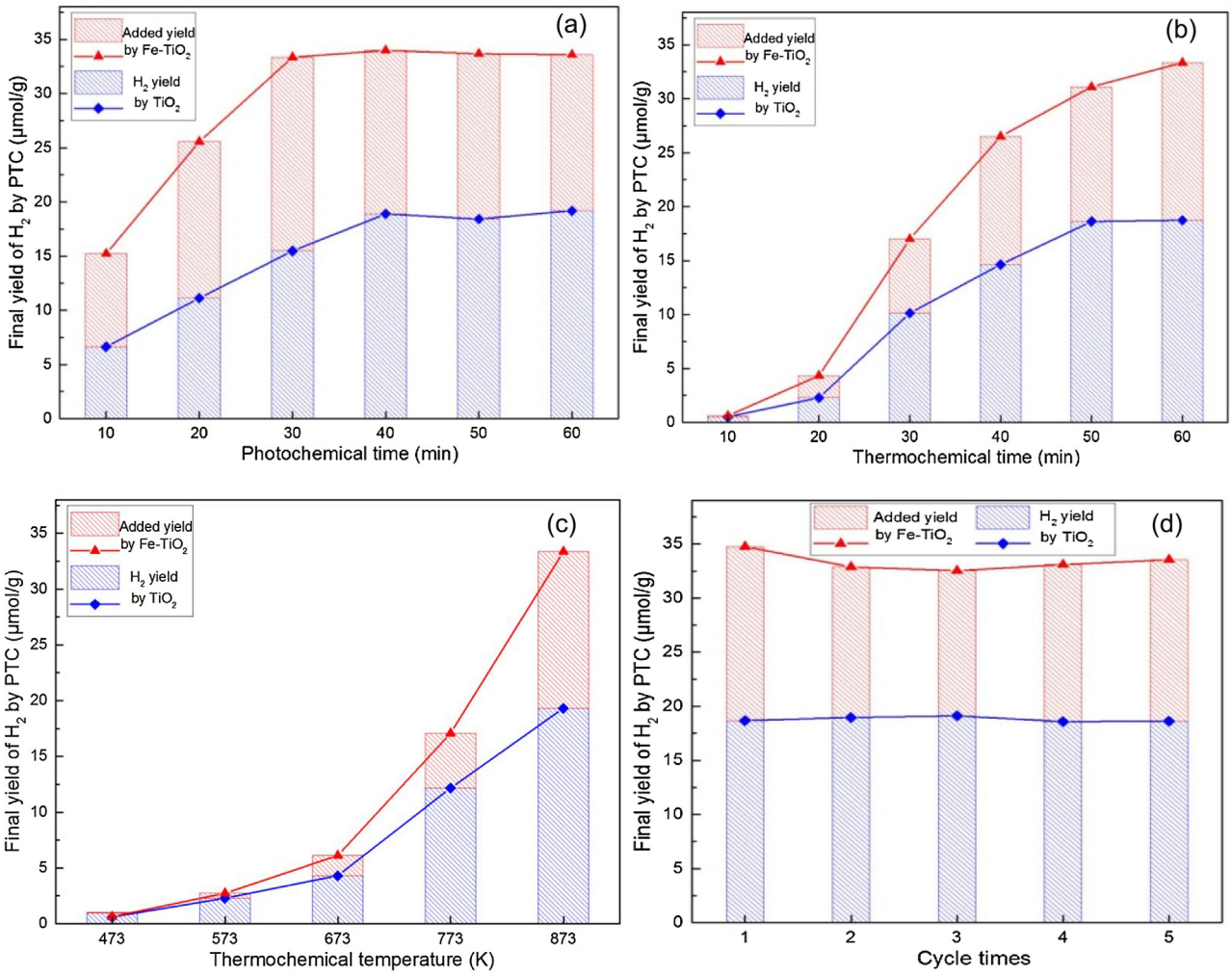


**Fig. 3.** $H_2$ production of several PTCs computed by mass: (a) the first series of samples were illuminated in a He atmosphere for 10, 20, 30, 40, 50 and 60 min and heated at 873 K for 1 h in a wet Ar atmosphere; (b) Fe-doped $TiO_2$ and $TiO_2$ were irradiated for 30 min and 40 min, respectively, and heated for 10 min, 20 min, 30 min, 40 min, 50 min and 60 min at 873 K; (c) Fe-doped $TiO_2$ was illuminated for 30 min and heated at different temperatures for 60 min. $TiO_2$ was illuminated for 40 min and heated at different temperatures for 50 min; (d) five successive PTCs were conducted: Fe-doped $TiO_2$ was illuminated for 30 min and heated at 873 K for 60 min, whereas $TiO_2$ was illuminated for 40 min and heated at 873 K for 50 min.

Little $H_2$ was generated at 473 K with either Fe-doped $TiO_2$ or $TiO_2$, whereas the $H_2$ yield increased observably from 573 K to 873 K. However, 873 K is the crystal transition temperature for $TiO_2$ (from anatase to rutile), which means that an additional uncontrollable factor is introduced at this temperature. Additionally, running the PTC at a higher temperature is uneconomical because this cycle was proposed to avoid high temperatures. Therefore, the experimental temperature was limited to 873 KAs shown in Fig. 3(d), five successive cycles were carried out. In the photo-step, Fe-doped $TiO_2$ was illuminated for 30 min and $TiO_2$ was illuminated for 40 min. In the thermo-step, Fe-doped $TiO_2$ was heated for 60 min at 873 K, whereas $TiO_2$ was heated for 50 min at 873 K. The $H_2$ yield was stable for both Fe-doped $TiO_2$ and $TiO_2$. The amount of produced $H_2$ was approximately 18.79 μmol/g for every cycle in the case of $TiO_2$. Additionally, the average amount of generated $H_2$, which was nearly 1.77 times greater than the amount of $H_2$ generated using $TiO_2$, was 33.36 μmol/g for every cycle in the case of Fe-doped $TiO_2$.

Interestingly, the $H_2$ production of PTC using Fe-doped $TiO_2$ was equivalent to 22.24 μmol/h/g at 873 K. To compare this result with $H_2$ production under photocatalysis, the representative results of $H_2$ production using doped $TiO_2$ are presented in Table 1. The selected samples were all $TiO_2$ and doped $TiO_2$with uncomplicated materials, treated without a sacrificial agent, under UV light. As shown, the $H_2$ productivities of Pt (0.3 wt%)-$TiO_2$and $TiO_2$ were3.33and 5.8 μmol/h/g using pure water under UV light in photocatalysis, which are less than the $H_2$ production of $TiO_2$ in the PTC [13,30,31]. The $H_2$ production of Fe (0.5 wt%)-$TiO_2$ was 22.24 μmol/h/g in the PTC, which is greater than the $H_2$ production of Ga-$TiO_2$ and Pt-B/Ti oxides in photocatalysis but less than that of Pt-$CaTiO_3$ [30,32,33]. Although the powers of the UV lamps differed somewhat, the results show that the novel PTC has adequate $H_2$ production that is comparable to that of photocatalysis using similar materials. In addition, the thermochemical step of PTC for water splitting was conducted in a wet Ar atmosphere, which was not overall water. The amount of generated $H_2$ may be increased if the ratio of vapour is increased.

### 3.2. Crystal structure and morphology

SEM was used to observe the morphology of the samples (Fig. 4). A comparison of Fig. 4(a) with Fig. 4(b) reveals that after heat treatment, undoped $TiO_2$ nanoparticles agglomerated more easily than Fe-doped $TiO_2$ nanoparticles [34]. TEM images of $TiO_2$ and 0.5 wt% Fe-doped $TiO_2$ are depicted in Fig. 5(a) and (b), respectively. Determining the average particle size was difficult because, as shown by a comparison of Fig. 5(a) with (b), primary nanoparticles are clearly

**Table 1**
$H_2$ production of PTC and photocatalysts for water splitting based on $TiO_2$.

| reaction material | reaction method | light source | aqueous reaction solution | $H_2$ production (μmol/h/g) | refs |
|---|---|---|---|---|---|
| Pt(0.3 wt%)-$TiO_2$ | photocatalysis | 400 W Hg | pure water | 3.33 | 23 |
| $TiO_2$ | photocatalysis | 360 W Hg | pure water | 5.8 | 24 |
| $TiO_2$ | PTC | 500 W Hg | wet Ar | 12.56 | 13 |
| Ga-$TiO_2$ | photocatalysis | UV | pure water | 20.86 | 16 |
| Pt-B/Ti oxide | photocatalysis | 150 W Hg | pure water | 22 | 23 |
| Fe-doped $TiO_2$ | PTC | 500 W Hg | wet Ar | 22.24 | / |
| Pt-$CaTiO_3$ | photocatalysis | 500 W Hg | pure water | 38 | 24 |

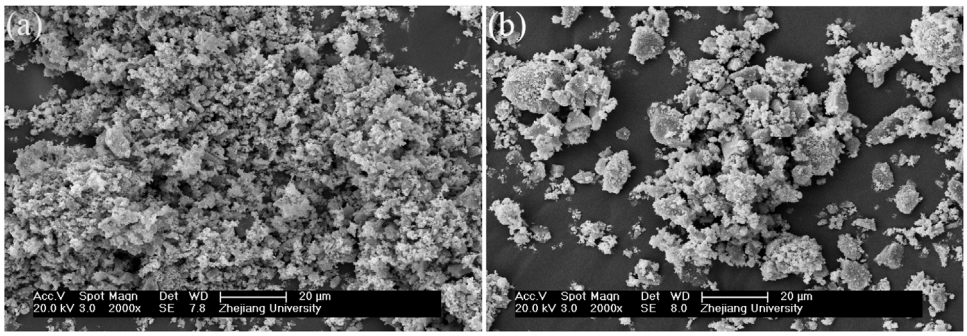


**Fig. 4.** SEM images of $TiO_2$ (a), 0.5 wt% Fe-doped $TiO_2$ (b).

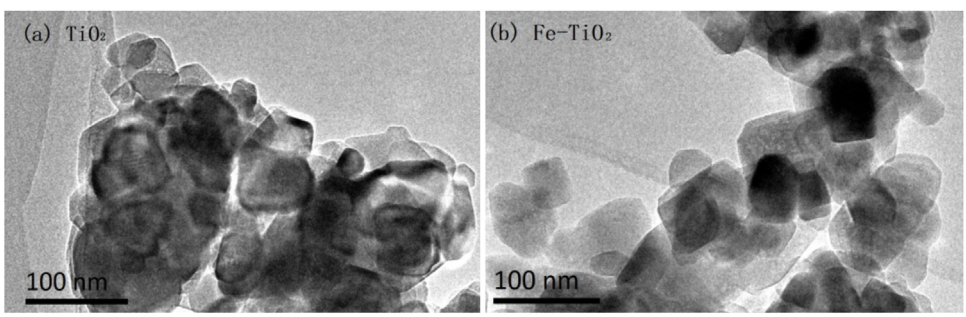


**Fig. 5.** TEM images of $TiO_2$ (a) and 0.5 wt% Fe-doped $TiO_2$ (b).

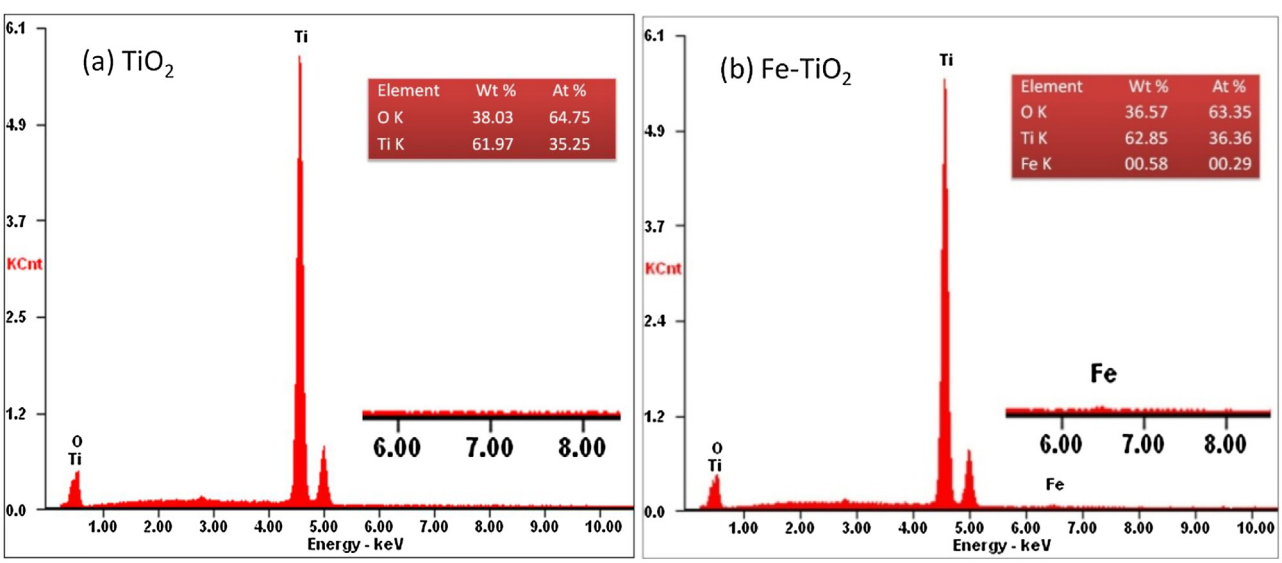


**Fig. 6.** EDAX patterns of $TiO_2$ (a) and 0.5 wt% Fe-doped $TiO_2$ (b).

distinguished only at the periphery of the aggregates. Therefore, the primary particle diameter of the prepared samples was estimated to be 30–70 nm. Undoped $TiO_2$ agglomerated more heavily than the 0.5 wt% Fe-doped $TiO_2$, consistent with the SEM observations [24]. The compositional analysis of the iron-doped $TiO_2$ nanoparticles was carried out by EDAX. The EDAX patterns for undoped and

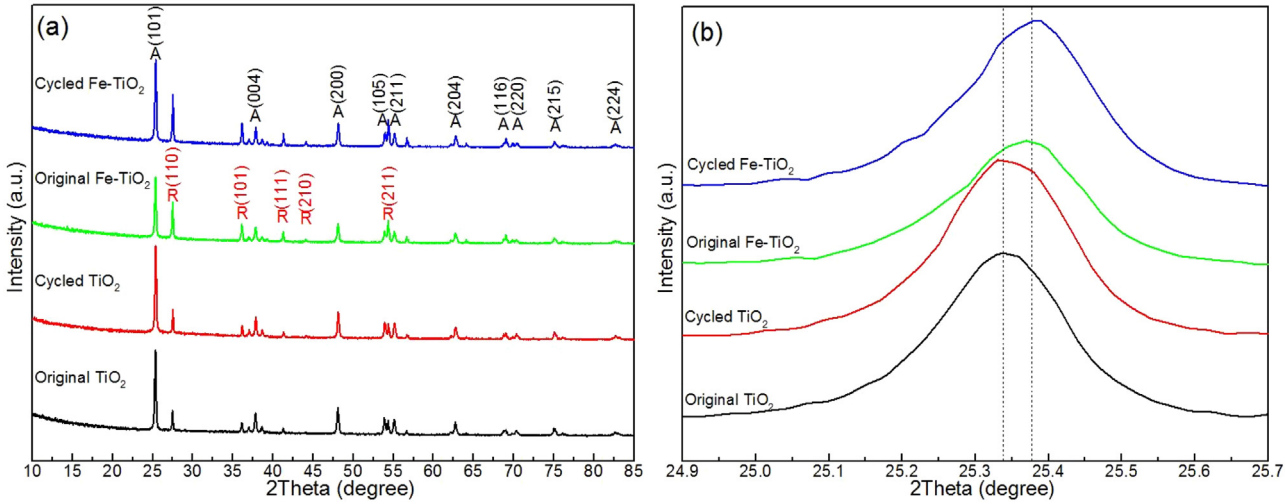


**Fig. 7.** XRD images: full patterns (a) and the anatase $TiO_2$ (101) peak (b) of $TiO_2$ and 0.5 wt% Fe-doped $TiO_2$ before and after PTC; the crystal faces are denoted by a black 'A' (anatase) and a red 'R' (rutile). (For interpretation of the references to colour in this figure legend, the reader is referred to the web version of this article.)

0.5 wt% Fe-doped $TiO_2$ are shown in Fig. 6(a) and (b), respectively. The data confirm that the Fe-doped $TiO_2$samples were composed of Fe, Ti and O. The mass ratio of Fe to Ti is approximately 0.58% in Fig. 6(b), which shows that the produced Fe-doped $TiO_2$ has the desired composition of iron with respect to titanium [35]. The BET surface area of $TiO_2$ decreased from 3.96 to 3.11 $m^2/g$ after cycled. However, the surface area of Fe-doped $TiO_2$ was 4.61 and 4.54 $m^2/g$ before and after cycle, which had few change. According to the BET result, Fe-doped $TiO_2$ have better sintering resistance, which was in accord with SEM and TEM result. [23]

XRD patterns of both Fe-doped $TiO_2$ and $TiO_2$ films were obtained before (original samples) and after (cycled samples) PTC experiments; the results are shown in Fig. 7. Both anatase and rutile phases are observed in the samples, where the respective crystal facets are denoted by a black 'A' and a red 'R', because the samples were preheated at 973 K for 4 h in a pure $O_2$ atmosphere [12,13]. No iron oxide or other material peaks were observed in the XRD patterns. This result shows that $Fe^{3+}$ may have high dispersion without significant change in $TiO_2$ [36]. In addition, the anatase $TiO_2$ (101) diffraction peak of Fe-doped $TiO_2$, which was the main peak in the patterns of the samples, was shifted to higher angles than those of $TiO_2$, as shown in Fig. 7(b). This result shows that $Fe^{3+}$ ions were doped into the $TiO_2$ lattice and that Fe—O—Ti bonds were formed, which led to the main peak shift [37]. We calculated the average crystallite size of undoped $TiO_2$ and Fe-doped $TiO_2$ samples by applying the Debye–Scherrer formula to the anatase $TiO_2$ (101) diffraction peaks. The results indicated average particle diameters of 53.5 nm (original $TiO_2$), 53.8 nm (cycled $TiO_2$), 38.4 nm (original Fe-doped $TiO_2$) and 38.6 nm (cycled Fe-doped $TiO_2$), in good agreement with the TEM results [35–37]. The crystallite size of Fe-doped $TiO_2$ is smaller than that of undoped $TiO_2$, which may prevent particle agglomeration, leading to well-defined nanocrystalline particles with a high surface area. Moreover, few differences were observed between the XRD patterns and crystallite sizes of the original and cycled samples. This lack of substantial changes suggests that the crystal structure and phase of the samples are stable and, thus, that the samples are well-suited to PTC.

### 3.3. PL, UV–vis and XPS analyses

According to the mechanism proposed in a previous study, at the superficial level, photo-excited electron-hole pairs act as important "fuel" for the photo-step in PTC [12,13]. Therefore, the separation efficiency of photogenerated electron-hole pairs is an important factor in the photoreaction of PTC. PL spectra are often used to study surface processes involving electron-hole pair recombination on semiconductors because PL emission mainly results from the recombination of free carriers [38,39]. To reveal the effect of Fe-doping on the separation of photogenerated electron-hole pairs, the PL spectra of the $TiO_2$ and Fe-doped $TiO_2$ samples were examined in the region from 340 to 640 nm under an excitation of 325 nm; the results are shown in Fig. 8. The PL spectra show that both samples exhibited signals upon irradiation at 325 nm. However, the incorporation of Fe into $TiO_2$ resulted in a weaker PL intensity than that of bare $TiO_2$, which suggests that the introduction of Fe into $TiO_2$ effectively suppressed the undesirable recombination of electrons and holes. This suppression is a consequence of $Fe^{3+}$ incorporated into $TiO_2$ functioning as an electron-trapping agent to promote electron-hole separation at low doping concentrations [40]. When the rate of recombination decreases, more photogenerated charge carriers can participate in the photochemical transformation, resulting in an enhancement of photoreaction activity.

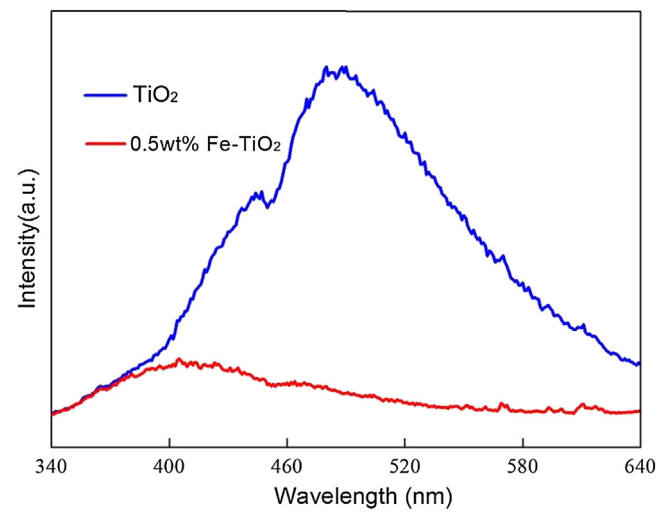


**Fig. 8.** PL patterns of $TiO_2$ and 0.5 wt% Fe-doped $TiO_2$.

The optical absorption properties of the undoped and Fe-doped $TiO_2$ samples and the optical energy band gap of the materials were

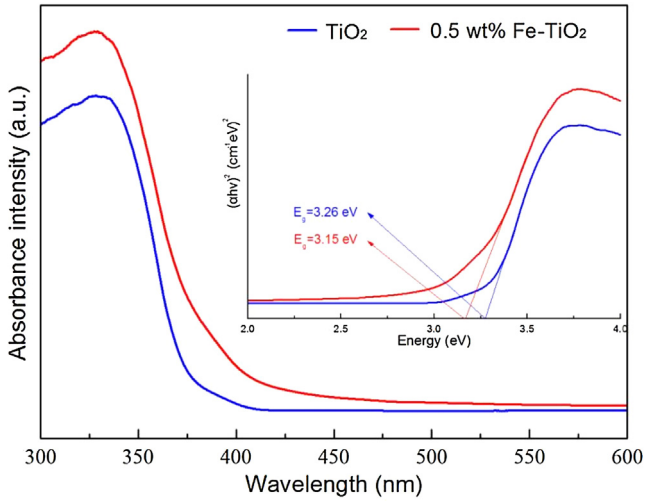


**Fig. 9.** UV–vis DRS patterns of $TiO_2$ and 0.5 wt% Fe-doped $TiO_2$. Inset: determination of the optical energy band gap.

examined by UV–vis DRS, as shown in Fig. 9. Obviously, the Fe-doped $TiO_2$ shows increased absorption and the absorption edge shows a red shift compared to that of undoped $TiO_2$. Moreover, the band-gap energy ($E_g$) of the $TiO_2$ and Fe-doped $TiO_2$ was recorded using the Kubelka-Munk equation, as shown in the inset of Fig. 10 [41]. The $E_g$ of Fe-doped $TiO_2$ is approximately 3.15 eV, which is smaller than that of undoped $TiO_2$ ($E_g$ = 3.26 eV).The red shift and narrower band gap of the Fe-doped $TiO_2$ sample both indicate that Fe-doped $TiO_2$ absorbed light with a wider wavelength range ($\lambda \leq 394$ nm) than that absorbed by $TiO_2$ ($\lambda \leq 380$ nm) [42]. A high-pressure mercury lamp has been equipped to radiate UVA light which ranges from 300 nm to 420 nm (Fig. S4). A wider absorption range means more electrons and holes are photogenerated, which improves the likelihood of an effective photoreaction. However, according to previous studies, the wider absorption range of Fe-doped $TiO_2$ is attributable to new energy levels introduced into the band gap of $TiO_2$ by $Fe^{2+}/Fe^{3+}$. Therefore, the red shift should arise the electronic transition from the dopant energy level ($Fe^{2+}/Fe^{3+}$) to the conduction band of $TiO_2$ [23].

To investigate the mechanism of the PTC based on Fe-doped $TiO_2$, X-ray photoelectron spectroscopy (XPS) spectra were employed to detect the chemical changes and the environmental changes of the atoms for three different states. As shown in Fig. 10, States A and B represent the Fe-doped $TiO_2$ sample before and after illumination, respectively, by UV light in a He atmosphere. State C was obtained from Fe-doped $TiO_2$ subjected to an integrated cycle in PTC. The results of the XPS peak differentiation imitating analysis of State A, B and C are shown in Fig. 10(a)–(c); the peaks centred at

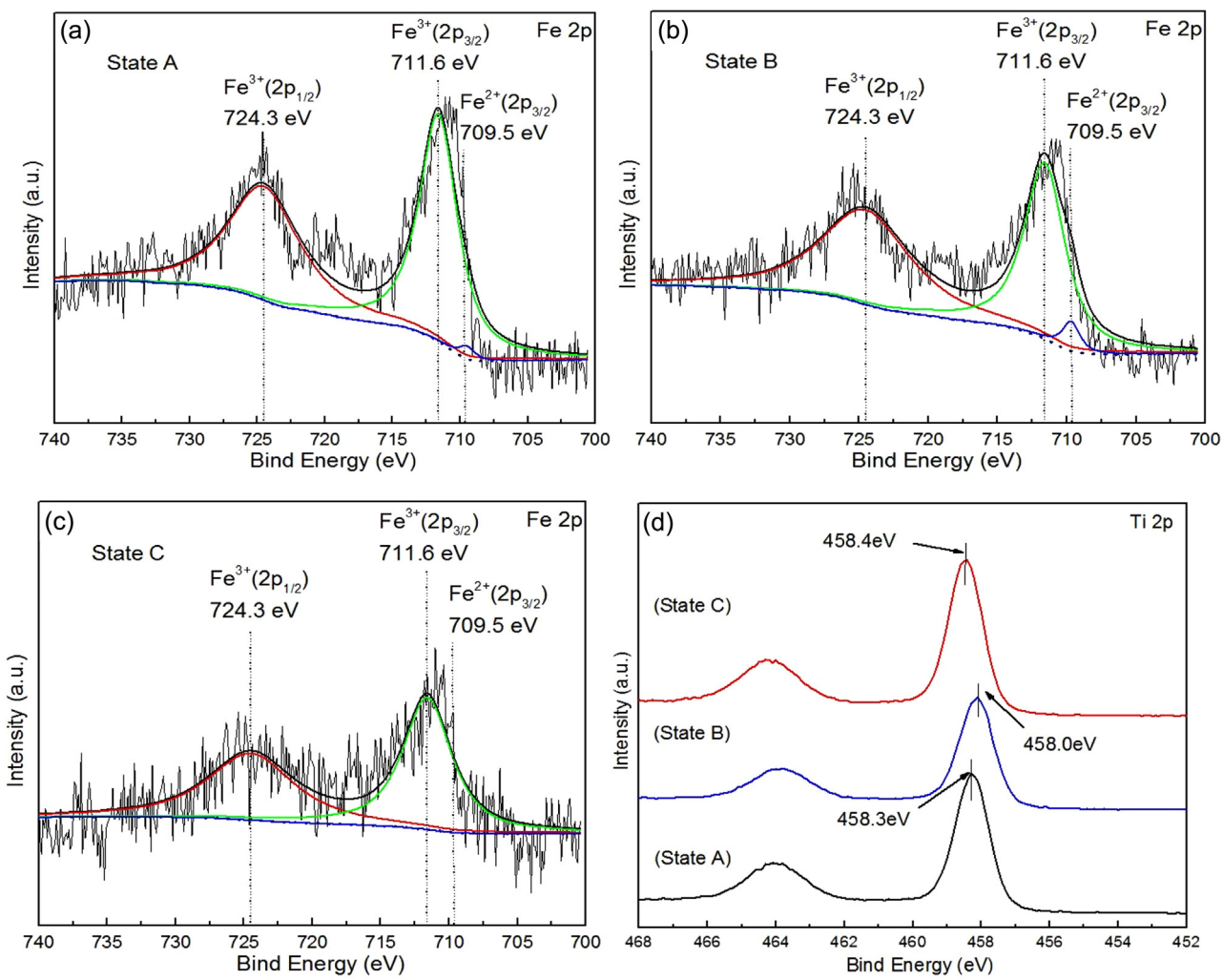


**Fig. 10.** XPS peak differentiation imitating analysis of the Fe 2p peak for (a) State A (before UV irradiation), (b) State B (after UV irradiation) and (c) State C (cycled) of Fe-doped $TiO_2$ powder. (d) XPS patterns of $TiO_2$ prepared at different states in the photo-thermochemical cycle.

**Table 2**
Total energies of the two possible, optimized configurations of Fe-doped surfaces.

| Corresponding figure | Style | Slab | $E_f$ (eV) |
|---|---|---|---|
| Fig. S5(a) | $Fe(Ti_{5C})$ | $Ti_{23}O_{47}Fe$ | 2.759432 |
| Fig. S5(b) | $Fe(Ti_{6C})$ | $Ti_{23}O_{47}Fe$ | 3.061971 |

724.3 eV and 711.6 eV can be assigned to $Fe^{3+}$ $2p_{1/2}$ and $Fe^{3+}$ $2p_{3/2}$, respectively. The peak located at 709.5 eV is assigned to $Fe^{2+}$ $2p_{3/2}$, respectively [24,42]. It is obvious that $Fe^{3+}$ was presence before, after UV irradiation and cycled sample, but there was hardly any $Fe^{2+}$ before UV irradiation and cycled. To compare the peaks of $Fe^{2+}$ in State A, B and C, the peak differentiation imitating result is more intuitive for the increase and decrease of $Fe^{2+}$. Fig. 10(d) shows that the binding energy of Ti $2p_{3/2}$ decreased from 458.3 eV to 458.0 eV from State A to State B and then returned to 458.4 eV at State C. And the shifts were beyond the experimental errors of ±0.2 eV. The phenomena can be attributed to the generation of $Ti^{3+}$ by UV light illumination [12,43]. The increase of $Fe^{2+}$ and $Ti^{3+}$ indicated that the $V_O$ may have been produced on the bond of Fe—O—Ti after UV illumination, and $V_O$ have been consumed after thermal step in PTC.

### 3.4. First-principles calculations

On the basis of the experimental characterization, we performed theoretical calculations for every step in the cycle to provide guidance for enhancing the reaction mechanism of the PTC. These calculations resulted in a deeper understanding of the effects of Fe-doping on $TiO_2$ throughout the whole cycle. The past works almost focus on the dopant energy level, which may narrow the band gap and expand the respond range of light. And the density of states (DOS) may be calculated to compare to experiments [23,28]. However, the defects formation and utilization have been studied in this work, and a possible completed pathway of reaction has been proposed. Previous reports have indicated that similar radii may be the reason for the easy substitution of Fe for Ti. Fe can substitute Ti atoms at two sites ($Ti_{5C}$ and $Ti_{6C}$) on the surface. The relaxed configurations resulting from the substitution of Ti atoms by Fe atoms are shown in Fig. S5; no substantial lattice distortion was observed. The total energies of the two possible optimized configurations of Fe-doped surfaces have been calculated; the results are shown in Table 2. The Fe ($Ti_{5C}$) site has been confirmed to be energetically favoured and was chosen as the representative configuration for subsequent calculations.

The Bader charge of Fe and Ti in Fe-doped $TiO_2$ at U = 5 eV and 8.2 eV for Fe 3d and Ti 3d have been calculated and listed in Table 3. If the Ti valence was +4 in clean Fe-doped $TiO_2$. The Bader charge analysis seems to overestimate the valance charge in the Ti cations by ~1.9. The supposed oxidation state of Fe was not +3 and +2, but +4 and +3 before and after $V_O$ formation. And it was inexplicable to compare it with experiments. Then it was supposed that the Fe doping leaded Ti valence to +3 so that the oxidation state of Fe was +3 and +2 before and after $V_O$ formation. The oxygen hole state may be generated on the Ti atom, which was common in metal ion doped metal oxide. And the oxidation state of Ti was +3, which was common oxidation state in $TiO_2$. However, to compare with experiments, the Bader charge method has been proven not precise by past works [44]. The population analysis has a certain randomness. As a result, the Bader charge is not necessarily an integer, the accuracy of its numerical value is not enough, but it can be used as a qualitative conclusion of the favorable basis. From another point of view, the increased Bader charge of Fe was much bigger than that of Ti before and after $V_O$ formation, which means that the Fe atom was more attractive to electrons when $V_O$ was formed.

**Table 4**
Calculated VO formation energies of different configurations on undoped and Fe-doped surfaces.

| Corresponding figure | Style | Position | Slab | $E_f$ (eV) |
|---|---|---|---|---|
| Fig. 11(a) | clean | $O_{2C}$ | $Ti_{23}O_{48}$ | 4.803 |
| Fig. 11(b) | clean | $O_{3C}{}^1$ | $Ti_{23}O_{48}$ | 5.529 |
| Fig. 11(c) | clean | $O_{3C}{}^2$ | $Ti_{23}O_{48}$ | 5.192 |
| Fig. 11(d) | clean | $O_{3C}{}^3$ | $Ti_{23}O_{48}$ | 5.019 |
| Fig. 11(e) | $Fe(Ti_{5C})$ | $O_{2C\text{-}p1}$ | $Ti_{23}O_{47}Fe$ | 0.373 |
| Fig. 11(f) | $Fe(Ti_{5C})$ | $O_{3C}{}^1$ | $Ti_{23}O_{47}Fe$ | 1.987 |
| Fig. 11(g) | $Fe(Ti_{5C})$ | $O_{3C}{}^2$ | $Ti_{23}O_{47}Fe$ | 2.365 |
| Fig. 11(h) | $Fe(Ti_{5C})$ | $O_{3C}{}^3$ | $Ti_{23}O_{47}Fe$ | 1.356 |
| Fig. 11(i) | $Fe(Ti_{5C})$ | $O_{2C\text{-}p2}$ | $Ti_{23}O_{47}Fe$ | 1.408 |
| Fig. 11(j) | $Fe(Ti_{5C})$ | $O_{2C\text{-}p3}$ | $Ti_{23}O_{47}Fe$ | 1.414 |
| Fig. 11(k) | $Fe(Ti_{5C})$ | $O_{2C\text{-}p4}$ | $Ti_{23}O_{47}Fe$ | 1.414 |

The formation of oxygen vacancies was considered the first step in the whole cycle. The $V_O$ formation energy was calculated by the following equation:

$$E_{vf} = E_{ds} + 1/2E_{O2} - E_{ps} \quad (5)$$

Where $E_{vf}$ represents the formation energy of $V_O$, whose positive value indicates that the reaction is endothermic; $E_{ds}$ and $E_{ps}$ represent the total energy of the vacancy surface and the clean surface, respectively; and $E_{O2}$ represents the total energy of a single oxygen molecule, which was calculated in a vacuum box of 10 × 10 × 10. Four different O sites ($O_{2C}$, $O_{3C}{}^1$, $O_{3C}{}^2$ and $O_{3C}{}^3$) are present on the surface [45]. The $V_O$ sites on the clean surface are shown in Fig. 11(a)–(d), and the $V_O$ sites on the vacancy surface are shown in Fig. 11(e)–(h). The results of calculations are shown in Table 4. Obviously, the $V_O$ formation energy of the Fe-doped surface is smaller than that of the clean surface. The reason might be the Fe doping made a local imbalance and the oxygen hole state may be formed in the sight of quantum chemistry. Additionally, the vacancies of $O_{2c}$ are apparently smaller than the others. However, four $O_{2C}$ sites ($O_{2C\text{-}p1}$, $O_{2C\text{-}p2}$, $O_{2C\text{-}p3}$ and $O_{2C\text{-}p4}$) were present on the surface, as shown in Fig. 11(e), (i)–(k). The $V_O$ of $O_{2c\text{-}p1}$ was the smallest among them, which means that $V_O$ was created most easily on these sites. The Fe-doped surface exhibits better performance than the undoped surface in the first step in PTC because of its ability to produce more $V_O$ sites.

Furthermore, extensive calculations were performed to study the adsorption of $H_2O$ molecules onto the defective surfaces. Four adsorption configurations are available for $H_2O$ molecules on the $V_O$ sites, as shown in Fig. 12. The vertical adsorption (V) in Fig. 12(i) and the horizontal adsorption (H) in Fig. 12(ii) are forms of physical adsorption. Additionally, the dissociated adsorption has two configurations (D1 and D2), as shown in Fig. 12(iii) and (iv). On both clean and Fe-doped surfaces ($Ti_{5C}$ substituted with Fe), four types of configurations were calculated at the $V_O$ sites of $O_{2C\text{-}p1}$ because $V_O$ ($O_{2C\text{-}p1}$) can be formed with the lowest energy. The models of adsorption and the adsorption energy results are shown in Fig. S6 and Table 5, respectively. Negative values indicate that the adsorptions are exothermic. Smaller negative values indicate stronger adsorption ability. The results of these calculations indicate that the

**Table 3**
Bader charge analysis of Fe and Ti in samples at U = 8.2 eV for Ti 3d and U = 5.0 eV for Fe 3d before and after $V_O$ formation.

| Bader charge (e) of Ti and Fe | $TiO_2$ | Defective $TiO_2$ | Fe-doped $TiO_2$ | Defective Fe-doped $TiO_2$ |
|---|---|---|---|---|
| Fe | / | / | 6.25 | 6.66 |
| Ti | 1.88 | 1.90 | 1.88 | 1.88 |

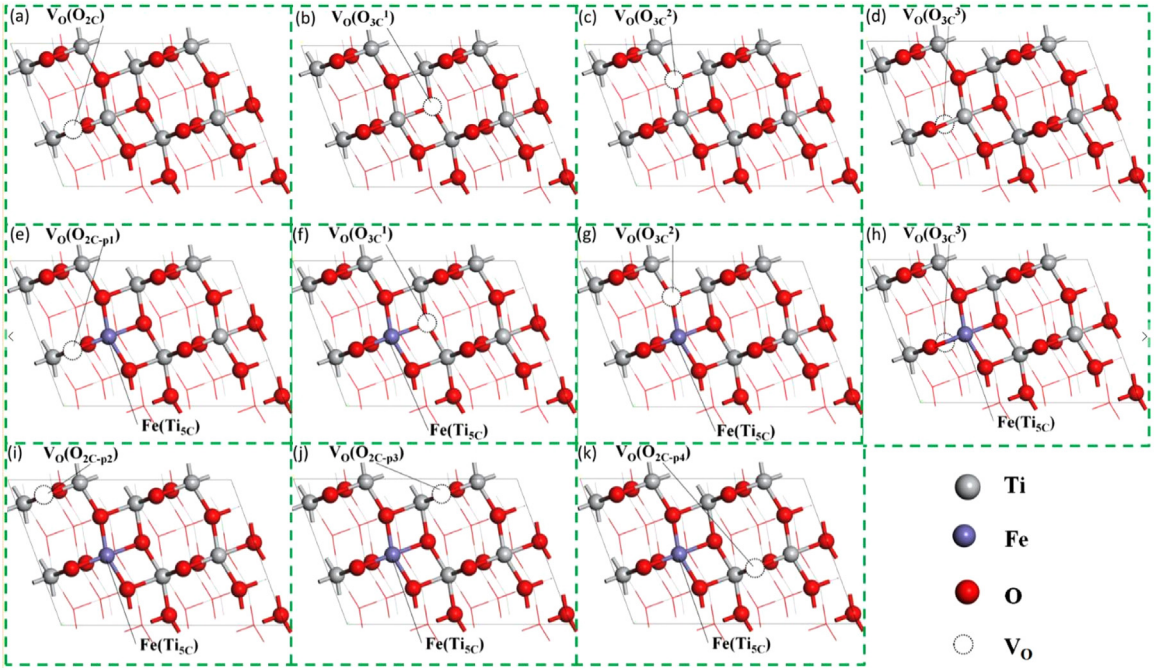


**Fig. 11.** Optimized structures for four configurations of O sites on the undoped (a, b, c, d) and Fe-doped (e, f, g, h) surfaces. Three different configurations of $V_O$ at $O_{2C}$ sites (i, j, k) are shown on the Fe-doped surface.

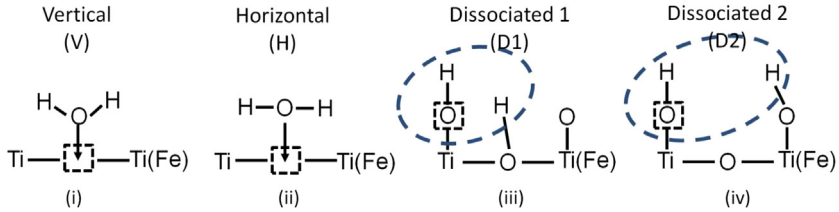


**Fig. 12.** Four adsorption configurations of $H_2O$ molecules on $V_O$.

**Table 5**
Calculated adsorption energies of different configurations on undoped and Fe-doped surfaces.

| Corresponding figure | Style | Initial configuration | Slab | $E_f$ (eV) |
|---|---|---|---|---|
| Fig. S6(a) | clean | Vertical | $Ti_{23}O_{48}$ | −0.9487 |
| Fig. S6(b) | clean | Horizontal | $Ti_{23}O_{48}$ | −1.0533 |
| Fig. S6(c) | clean | Dissociated 1 | $Ti_{23}O_{48}$ | −0.9227 |
| Fig. S6(d) | clean | Dissociated 2 | $Ti_{23}O_{48}$ | −1.0827 |
| Fig. S6(e) | $Fe(Ti_{5C})$ | Vertical | $Ti_{23}O_{47}Fe$ | −4.9484 |
| Fig. S6(f) | $Fe(Ti_{5C})$ | Horizontal | $Ti_{23}O_{47}Fe$ | −5.0923 |
| Fig. S6(g) | $Fe(Ti_{5C})$ | Dissociated 1 | $Ti_{23}O_{47}Fe$ | −5.2098 |
| Fig. S6(h) | $Fe(Ti_{5C})$ | Dissociated 2 | $Ti_{23}O_{47}Fe$ | −5.6339 |

$V_O$ sites on the Fe-doped surface have better adsorption power than the $V_O$ sites on the clean surface. The D2 configuration is the most likely pathway and was thus adopted for the calculation of whole reactions (including desorption of $H_2$) on the defective undoped and Fe-doped surfaces [46].

### 3.5. Enhanced mechanism

Experimental results of XRD, PL and UV–vis indicate that $Fe^{3+}$ incorporated into $TiO_2$ can act as an electron-trapping agent, which may improve the separation of electron-hole pairs and produce more electron-hole pairs for the first step of the PTC. According to the XPS results, the $V_O$ may have been produced on the bond of Fe—O—Ti after UV illumination. For the reason that the $V_O$ formation energy was smaller at the bond of Fe—O—Ti, the $V_O$ could be easier formed in Fe-doped $TiO_2$. Moreover, the $V_O$ production is attributed to the lower formation energy for $V_O$ on the Fe-doped surface, which would promote the reactions in the PTC. Then the $V_O$ could absorb the $H_2O$ molecule and be consumed for water splitting in the second thermal step. Finally, $H_2$ has been produced after desorption on the material surface.

From a further DFT study, a possible reaction pathway was determined for the second step, as shown in Fig. 12. The adsorption (D2) of $H_2O$ onto and desorption of $H_2$ from the $V_O$ sites of clean and Fe-doped surfaces are shown in Fig. 13(a) and (b), respectively. As shown in Table 6, the reaction in the second step of the PTC can be divided into 4 sub-steps: a $H_2O$ molecule ($H_2O$ (g)) is attracted by a $V_O$ site on the surface. The $H_2O$ molecule ($H_2O$ (ads)) is adsorbed onto $V_O$ in the D2 configuration, forming two unstable hydroxyls ($HO^*$ ($V_O$) and $H^*$ ($O_{2C}$)). The $H_2O$ molecule is then dissociated into

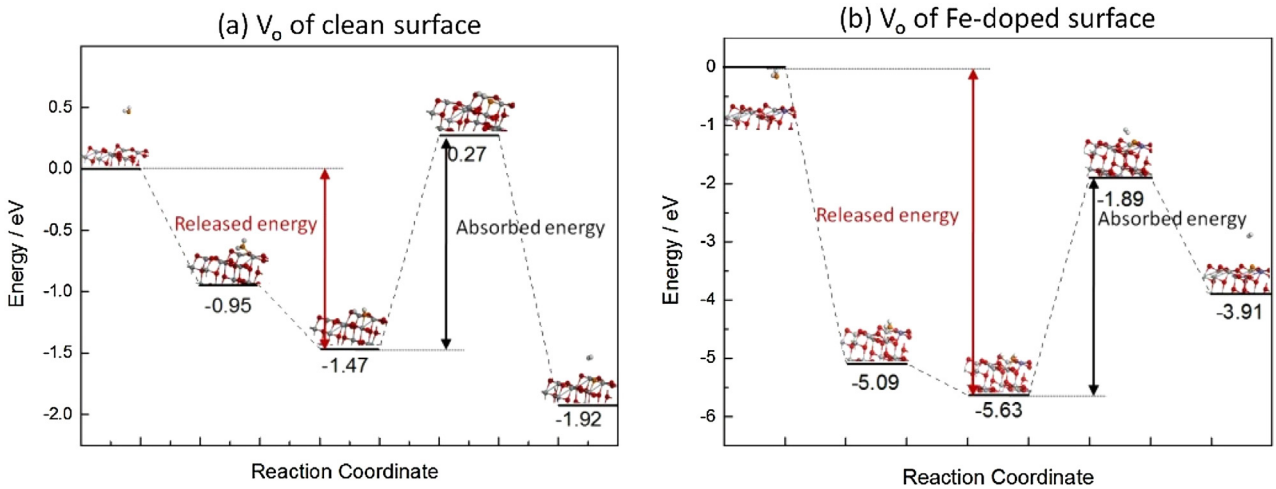


**Fig. 13.** Energy profiles and optimized configurations of second reaction steps on an undoped surface (a) and a Fe-doped surface (b) in PTC.

**Table 6**
Enhanced mechanism of the second step in the PTC on anatase (101).

| Reaction step | Relative energy (eV) on the undoped surface | Relative energy (eV) on the Fe-doped surface |
|---|---|---|
| $H_2O$ (g) → $H_2O$ (ads) | −0.95 | −5.09 |
| $H_2O$ (ads) + $V_O$ → HO* ($V_O$) + H* ($O_{2C}$) | −1.47 | −5.63 |
| HO* ($V_O$) + H($O_{2C}$)* → $H_2$ (ads) + $O_{2C}$ | 0.27 | −1.89 |
| $H_2$ (ads) → $H_2$ (g) | −1.92 | −3.91 |

$H_2$ (ads), and the $V_O$ is consumed by the oxygen of $H_2O$ on the $O_{2C}$ site. Finally, the $H_2$ (g) is desorbed from the surface. The calculations of the transient state also indicate that the absorbed energy is bigger than the released energy of adsorption at the $V_O$ sites of the clean surface. Conversely, the released energy of adsorption is bigger than the absorbed energy at $V_O$ sites of the Fe-doped surface. The $H_2$ on the $V_O$ of the Fe-doped surface may be easier to dissociate from the surface, which is important for the improvement of $H_2$ production.

## 4. Conclusions and outlook

For an in-depth study of the mechanism of the PTC, several experiments were performed with undoped and Fe-doped $TiO_2$, both of which were prepared via a sol-gel method. The results of the experiments indicate that the Fe-doped $TiO_2$ could improve the production of $H_2$ in the PTC. Moreover, the production of $H_2$ via the PTC using Fe-doped $TiO_2$ is adequate and comparable with that of photocatalysis under similar conditions. Additionally, the characterization of undoped and Fe-doped $TiO_2$ indicates that Fe ions may lead to lighter agglomeration, which is beneficial for cycling stability. More photoinduced electron-hole pairs are made available with less recombination because $Fe^{3+}$ incorporated into $TiO_2$ can function as an electron-trapping agent. On the basis of the XRD results and discovery of Fe—O—Ti bonds on the surface of Fe-doped $TiO_2$, the formation and consumption of $V_O$ on Fe—O—Ti bond was indicated by XPS results. Then a calculation model for Fe-doped $TiO_2$ was constructed. DFT calculations were completed for the whole cycle, from $V_O$ formation to $H_2$ desorption. The Fe-doped surface has a low $V_O$ formation energy, stronger $H_2O$ adsorption ability and smaller energy for desorption of $H_2$. The DFT calculations verified the better performance of the Fe-doped surface on the molecular level. Finally, we proposed an enhanced mechanism that describes every reaction step of the PTC in detail. Materials doped with metal ions are widely used in catalysis. Fe-doped $TiO_2$ shows improvements in both PTC and photocatalysis, which indicates that it may have similar mechanisms. Additional comparative studies between PTC and photocatalysis should be undertaken to clarify the mechanism and improve production. Despite the limitations of the current work, the PTC is a promising approach, especially if efforts are made to improve the cycle materials.

## Acknowledgement

This work was financially supported by National Natural Science Foundation of China (51276170). The authors gratefully acknowledge the support.

## Appendix A. Supplementary data

Supplementary data associated with this article can be found, in the online version, at http://dx.doi.org/10.1016/j.apcatb.2016.11.027.

## References

[1] J.A. Turner, Science 305 (2004) 972–974.
[2] S.E. Hosseini, M.A. Wahid, Renew. Sustain. Energ. Rev. 57 (2016) 850–866.
[3] P. Favuzza, C. Felici, L. Nardi, P. Tarquini, A. Tito, Appl. Catal. B-Environ. 105 (2011) 30–40.
[4] F. Yilmaz, M.T. Balta, R. Selbaş, Renew. Sustain. Energ. Rev. 56 (2016) 171–178.
[5] J.R. McKone, N.S. Lewis, H.B. Gray, Chem. Mater. 26 (2014) 407–414.
[6] M.S. Faber, S. Jin, Energy Environ. Sci. 7 (2014) 3519–3542.
[7] W.C. Chueh, C. Falter, M. Abbott, D. Scipio, P. Furler, S.M. Haile, A. Steinfeld, Science 330 (2010) 1797–1801.
[8] P. Furler, J.R. Scheffe, A. Steinfeld, Energy Environ. Sci. 5 (2012) 6098–6103.
[9] P.G. Loutzenhiser, A. Meier, A. Steinfeld, Materials 3 (2010) 4922–4938.
[10] D. Arifin, V.J. Aston, X. Liang, A.H. McDaniel, A.W. Weimer, Energy Environ. Sci. 5 (2012) 9438–9443.
[11] Y. Zhang, Q. Zhu, X. Lin, Z. Xu, J. Liu, Z. Wang, J. Zhou, K. Cen, Appl. Energy 108 (2013) 1–7.
[12] Y. Zhang, C. Xu, J. Chen, X. Zhang, Z. Wang, J. Zhou, K. Cen, Appl. Energy 156 (2015) 223–229.
[13] Y. Zhang, J. Chen, C. Xu, K. Zhou, Z. Wang, J. Zhou, K. Cen, Int. J. Hydrogen Energy 41 (2016) 2215–2221.
[14] F. Akira, H. Kenichi, Nature 238 (1972) 37–38.
[15] H.J. Chae, I.-S. Nam, S.-W. Ham, S.B. Hong, Appl. Catal. B-Environ. 53 (2004) 117–126.

[16] H. Sun, Y. Bai, H. Liu, W. Jin, N. Xu, G. Chen, B. Xu, J. Phys Chem C 112 (2008) 13304–13309.
[17] H. Sun, S. Wang, Energy Fuel. 28 (2014) 22–36.
[18] Y. Ma, X. Wang, Y. Jia, X. Chen, H. Han, C. Li, Chem. Rev. 114 (2014) 9987–10043.
[19] H. Sun, R. Ullah, S. Chong, H.M. Ang, M.O. Tade, S. Wang, Appl. Catal. B-Environ. 108–109 (2011) 127–133.
[20] X. Chen, S. Shen, L. Guo, S.S. Mao, Chem. Rev. 110 (2010) 6503–6570.
[21] Q. Zhang, G. Rao, J. Rogers, C. Zhao, L. Liu, Y. Li, J. Chem. Eng. 271 (2015) 180–187.
[22] G. Rao, Q. Zhang, H. Zhao, J. Chen, Y. Li, J. Chem. Eng. 302 (2016) 633–640.
[23] J. Ma, H. He, F. Liu, Appl. Catal. B-Environ. 179 (2015) 21–28.
[24] M. Crişan, M. Răileanu, N. Drăgan, D. Crişan, A. Ianculescu, I. Niţoi, P. Oancea, S. Şomăcescu, N. Stănic&#x0103, B. Vasile, C. Stan, Appl. Catal. A-Gen. 504 (2015) 130–142.
[25] T. Harifi, M. Montazer, Appl. Catal. A-Gen. 473 (2014) 104–115.
[26] S.-m. Chang, W.-s. Liu, Appl. Catal. B-Environ. 156–157 (2014) 466–475.
[27] K. Yang, Y. Zhang, Y. Li, P. Huang, X. Chen, W. Dai, X. Fu, Appl. Catal. B-Environ. 183 (2016) 206–215.
[28] H. Li, F. Ren, J. Liu, Q. Wang, Q. Li, J. Yang, Y. Wang, Appl. Catal. B-Environ. 172–173 (2015) 37–45.
[29] L. Liu, Y. Jiang, H. Zhao, J. Chen, J. Cheng, K. Yang, Y. Li, ACS Catal. 6 (2016) 1097–1108.
[30] M. Ni, M.K.H. Leung, D.Y.C. Leung, K. Sumathy, Renew. Sustain. Energ. Rev. 11 (2007) 401–425.
[31] F.E. Osterloh, Chem. Mater. 20 (2008) 35–54.
[32] P. Ritterskamp, A. Kuklya, M.A. Wustkamp, K. Kerpen, C. Weidenthaler, M. Demuth, Angew. Chem. Int. Ed. 46 (2007) 7770–7774.
[33] J. Xing, W.Q. Fang, H.J. Zhao, H.G. Yang, J. Chem. Asian 7 (2012) 642–657.
[34] A. Molea, V. Popescu, N.A. Rowson, I. Cojocaru, A. Dinescu, A. Dehelean, M. Lazăr, Ind. Eng. Chem. Res. 54 (2015) 7346–7351.
[35] Z. Sayyar, A. Akbar Babaluo, J.R. Shahrouzi, Appl. Surf. Sci. 335 (2015) 1–10.
[36] M. Khan, S. Woo, O. Yang, Int. J. Hydrogen Energy 33 (2008) 5345–5351.
[37] T. Sun, E. Liu, J. Fan, X. Hu, F. Wu, W. Hou, Y. Yang, L. Kang, J. Chem. Eng. 228 (2013) 896–906.
[38] L. Jing, M. Wang, X. Li, R. Xiao, Y. Zhao, Y. Zhang, Y.-M. Yan, Q. Wu, K. Sun, Appl. Catal. B-Environ. 166–167 (2015) 270–276.
[39] E. Cui, G. Lu, Int. J. Hydrogen Energy 39 (2014) 7672–7685.
[40] S.D. Delekar, H.M. Yadav, S.N. Achary, S.S. Meena, S.H. Pawar, Appl. Surf. Sci. 263 (2012) 536–545.
[41] S.S. Lee, H. Bai, Z. Liu, D.D. Sun, Water Res. 47 (2013) 4059–4073.
[42] S. Wang, J.S. Lian, W.T. Zheng, Q. Jiang, Appl. Surf. Sci. 263 (2012) 260–265.
[43] J.Z. Zhao, W.Q. Xing, Y. Li, K. Lu, Solvothermal synthesis and visible light absorption of anatase $TiO_2$, Mater. Lett. 145 (2015) 332–335.
[44] W. Cen, Y. Liu, Z. Wu, H. Wang, X. Weng, Phys. Chem. Chem. Phys. 14 (2012) 5769–5777.
[45] Q.L. Chen, B. Li, G. Zheng, K.H. He, A.S. Zheng, Physica B 406 (2011) 3841–3846.
[46] Ö. Yalçın, I. Önal, Int. J. Hydrogen Energy 39 (2014) 19563–19569.